Supporting Information

Dual Synergistic Modulation of Photo-Induced Electron Transfer Processes Between Molecules and Gold Nanopillars for Ultrasensitive Plasmon-Enhanced Raman Scattering

Iris B. Ansah,[†,‡,#] Daniel Aranda,[¦,#] Ho Sang Jung,[†] Sung-Gyu Park,[†] Mijeong Kang,[§,] Juan C. Otero,[¬,*] and Dong-Ho Kim[†,‡,*]*

[†]Nano-Bio Convergence Department, Korea Institute of Materials Science (KIMS), Changwon, Gyeongnam 51508, Republic of Korea

[‡]Advanced Materials Engineering Division, University of Science and Technology (UST), Daejeon 34113, Republic of Korea

[¦]Istituto di Chimica dei Composti Organometallici, Consiglio Nazionale delle Ricerche (ICCOM-CNR), 56124, Pisa, Italy.

[§]Department of Cogno-Mechatronics Engineering, Pusan National University (PNU), Busan 46241, Republic of Korea

[¬]Universidad de Málaga, Andalucía Tech, Facultad de Ciencias, Departamento de Química Física, 29071-Málaga, Spain

[#] These authors contributed equally.

Experimental methods

Computational details

Electronic structure calculations were performed under density functional theory (DFT) and its time-dependent extension (TD-DFT), as implemented in the Gaussian16 suite of programs,[1] at the B3LYP/LanL2DZ and M06-HF/LanL2DZ levels of theory. Vibrational wavenumbers and normal Raman intensities of PQ^{2+} were calculated with the B3LYP functional[2-4] (Figures S1 and S2). However, this functional cannot accurately predict the electronic properties of the charge transfer states because it usually underestimates their energies. Instead, we carried out TD excited-state calculations using the long-range-corrected M06-HF functional.[5,6] The electron-core potential LanL2DZ basis set was used.[7-10]

Normal Raman intensities (Figure S1) were estimated from the differential Raman scattering cross sections using the equation:[11]

$$\left(\frac{d\sigma}{d\Omega}\right)_i = (2\pi)^4 \cdot \frac{h}{8\pi^2 c\bar{\nu}_i} \cdot \frac{\left(\bar{\nu}_0 - \bar{\nu}_i\right)^4}{1 - exp(-hc\bar{\nu}_i/k_B T)} \cdot \frac{S_i}{45}$$

where $\bar{\nu}_0$ and $\bar{\nu}_i$ are the wavenumbers of the incident light and the i^{th} normal mode, c is the speed of light, h is Planck's constant, k_B is Bolztmann's constant, T is the temperature, and S_i is the static Raman scattering factor provided by the B3LYP/LanL2DZ calculations.

Raman spectra in resonance with a single excited state were computed using the well-known relation[11]

$$I_i \propto \bar{\nu}_i^2 \Delta k_i^2$$

where the intensity of a particular mode I_i depends on its vibrational wavenumber $\bar{\nu}_i$ and dimensionless displacement Δk_i. These resonant Raman intensities were computed using the FCclasses3 code[12] and the gradients calculated at the Frank–Condon point, which is usually known as the vertical gradient or linear coupling model approach. Finally, the calculated spectra were constructed from I_i by convoluting the bands with a 10 cm^{-1} full-width at half-maximum (FWHM) Lorentzian.

The functionalized interface was modelled in the electronic structure calculations as Au_n^q–X^-–PQ^{2+} supermolecules, where X^- is either $[AuCl_4]^-$ or $[Au(CN)_2]^-$ and Au_n^q are linear Au clusters

with different numbers of atoms n (3, 5, 7, 8) and different charges q (−1, +1 for odd values of n, and 0 for n = 8) (see Figure S3 for some examples). The effect of the electrode potential on the electronic structure of the interface was simulated through the $q_{eff} = q/n$ parameter that modulates the electron density on the Au_n^q clusters and would be the microscopic analogue of the surface excess of charge of an electrode. To keep the metal–adsorbate interaction as similar as possible among the molecular models, X^-–PQ^{2+} systems were bonded to a single terminal atom of the linear Au_n^q nanowires (Figure S3). Despite its simplicity, this methodology has proven useful in analyzing the complex behavior shown by the SERS of benzene-like systems.[13-17]

Au_n^q–X^-–PQ^2 supermolecules were optimized in two steps. Au_n^q–X^- binary systems were firstly optimized with restricted symmetry (C_{4v} and C_{2v} for $[AuCl_4]^-$ and $[Au(CN)_2]^-$, respectively). In the second step, PQ^{2+} was added to the Au_n^q–X^- optimized geometries, maintaining the stick-like structure of Au_n^q in each Au_n^q–X–PQ^{2+} system and enabling the remaining coordinates to be relaxed. The final optimized structures correspond to X–PQ^{2+} chemical species bonded to a single atom of the Au electrode, therefore simulating X–PQ^{2+} adsorbed parallel to the metal surface, in agreement with the predicted flat orientation of $[Au(CN)_2]^-$ on Au.[18]

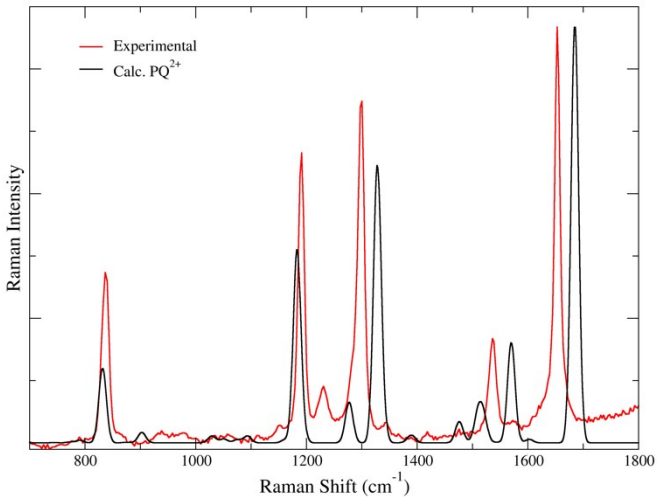

Figure S1. Experimental (red, 785 nm excitation) and B3LYP/LanL2DZ calculated (black) normal Raman spectra of PQ^{2+} (unscaled wavenumbers).

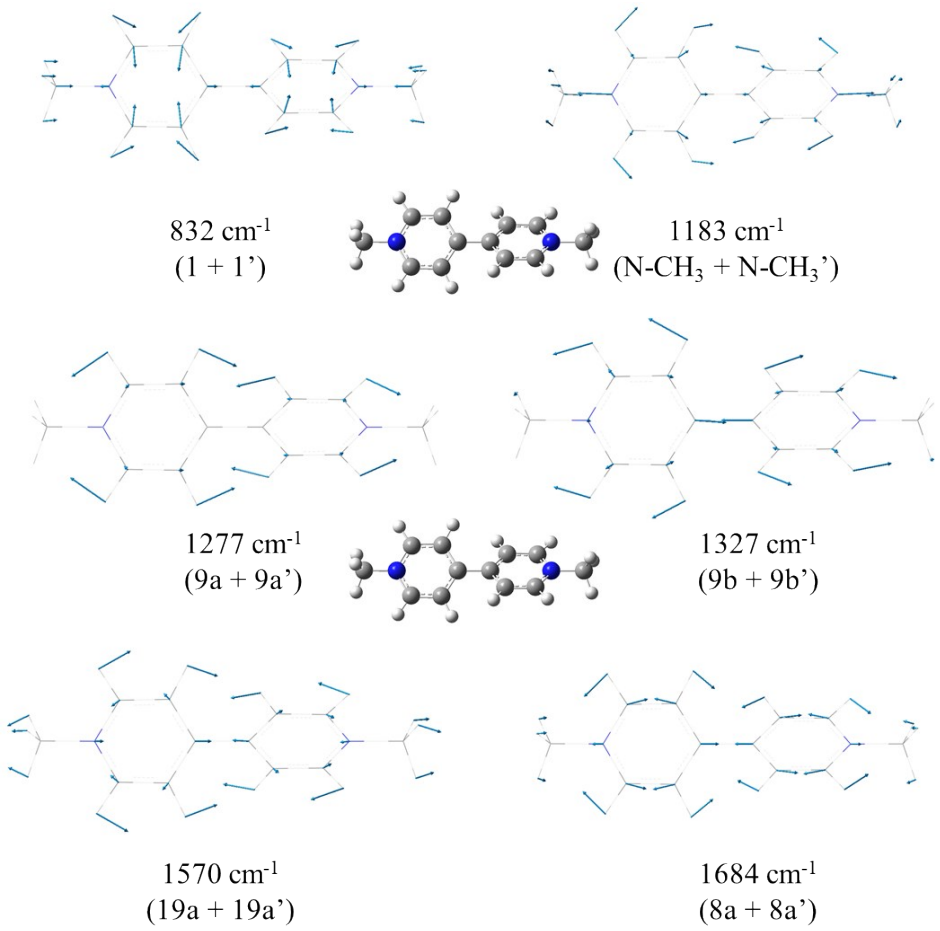

Figure S2. B3LYP/LanL2DZ calculated displacement vectors of the main normal modes recorded in the normal Raman spectrum of PQ^{2+} (unscaled wavenumbers). Ball-and-stick molecular models are included for reference. The calculated frequencies and the assignment according to Wilson's nomenclature are also displayed. Note that all the relevant modes correspond to symmetric combinations of two vibrations located in each aromatic ring.

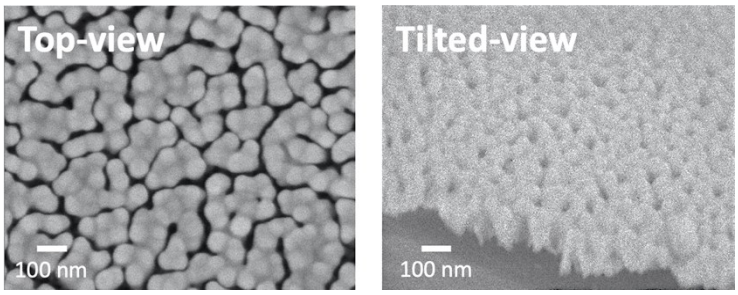

Figure S3. Scanning electron microscopy images of Au nanopillar substrates.

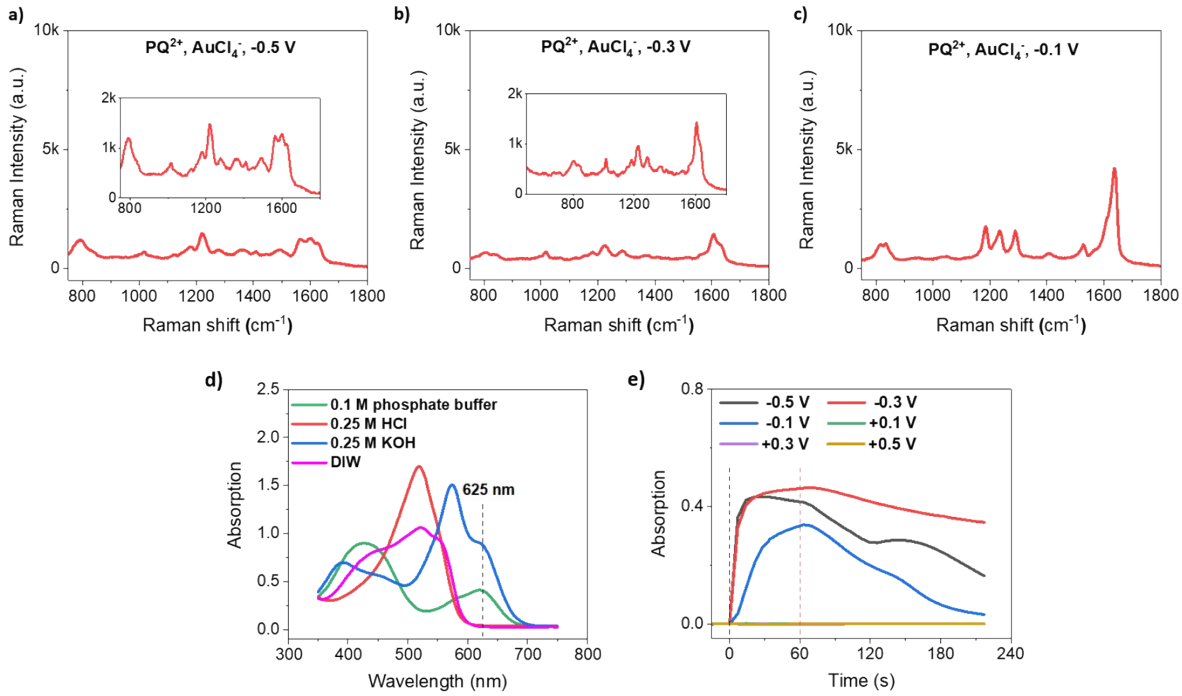

Figure S4. EC-SERS spectra of PQ^{2+} (5 µM) in the presence of $AuCl_4^-/Cl^-$ (1 mM/0.1 M) at negative potentials of (a) −0.5, (b) −0.3 and (c) −0.1 V, showing bands of decomposition products. (d) UV–VIS absorption spectra of pH indicator solution (product from EMD Millipore, catalogue number: 1091750100) measured in phosphate buffer solution, hydrochloric acid (HCl), potassium hydroxide (KOH) solutions and deionized water (DIW). The reference wavelength used to monitor pH changes as potentials were applied was 625 nm. (e) UV–VIS absorption spectra of the four mentioned solutions of the pH indicator at a fixed wavelength of 625 nm over time at constant potentials of +0.5, +0.3, +0.1, −0.1, −0.3 and −0.5 V applied for 60 s. The black and red dashed lines represent the start and stop range of applied potentials, respectively. At −0.5, −0.3 and −0.1 V, the absorption intensities abruptly increase when the potential is applied (0 s), showing that the pH at the electrode surface increases because of oxygen reduction.

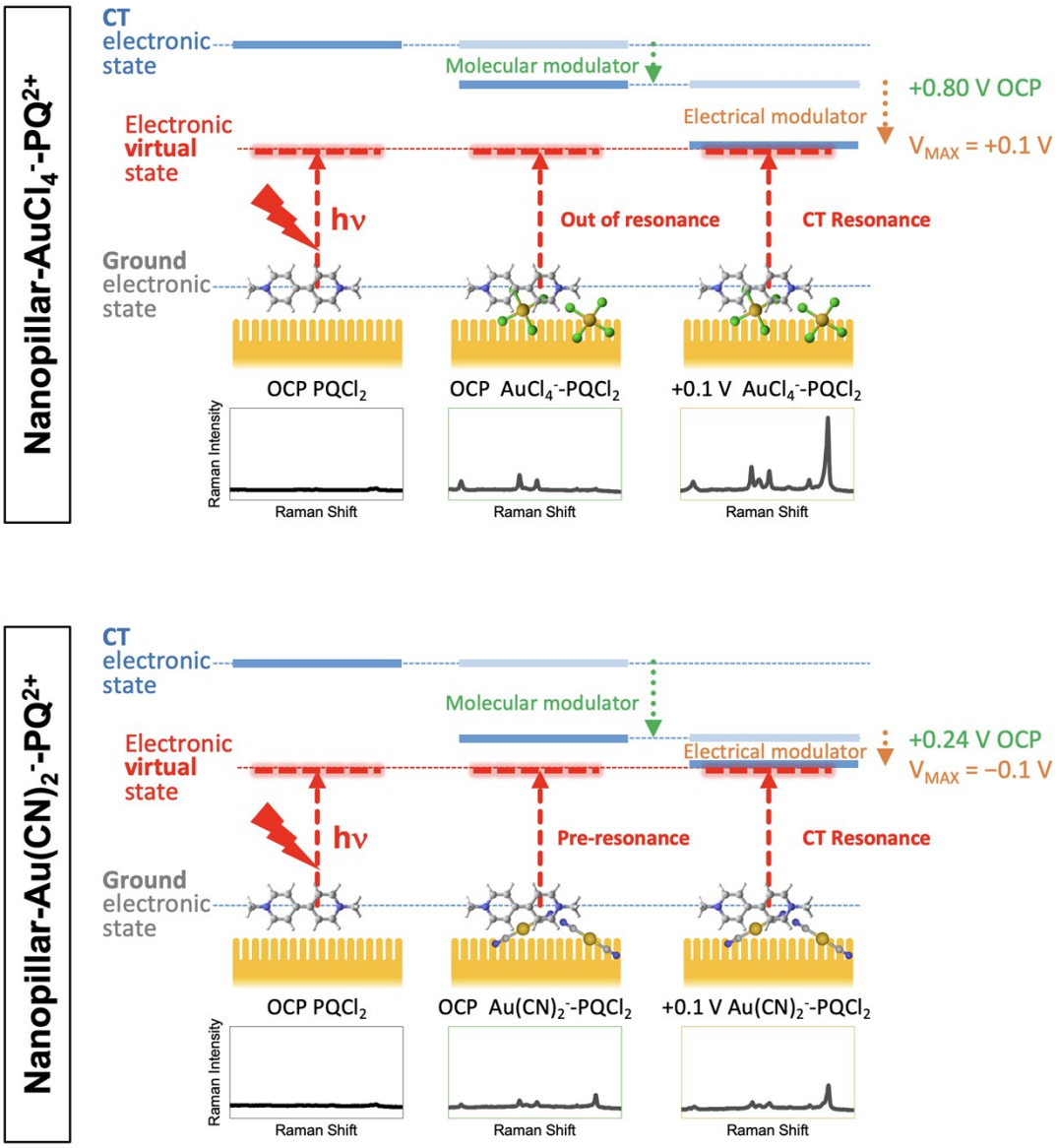

Figure S5. Schemes showing the differentiated effect of molecular (anionic complexes) and electrical (electrode potential) modulators in tuning the relative energies between the ground and CT excited electronic states of nanopillar–$AuCl_4^-$–PQ^{2+} (top) and nanopillar–$Au(CN)_2^-$–PQ^{2+} (bottom) interfaces involved in the photo-induced resonant CT processes.

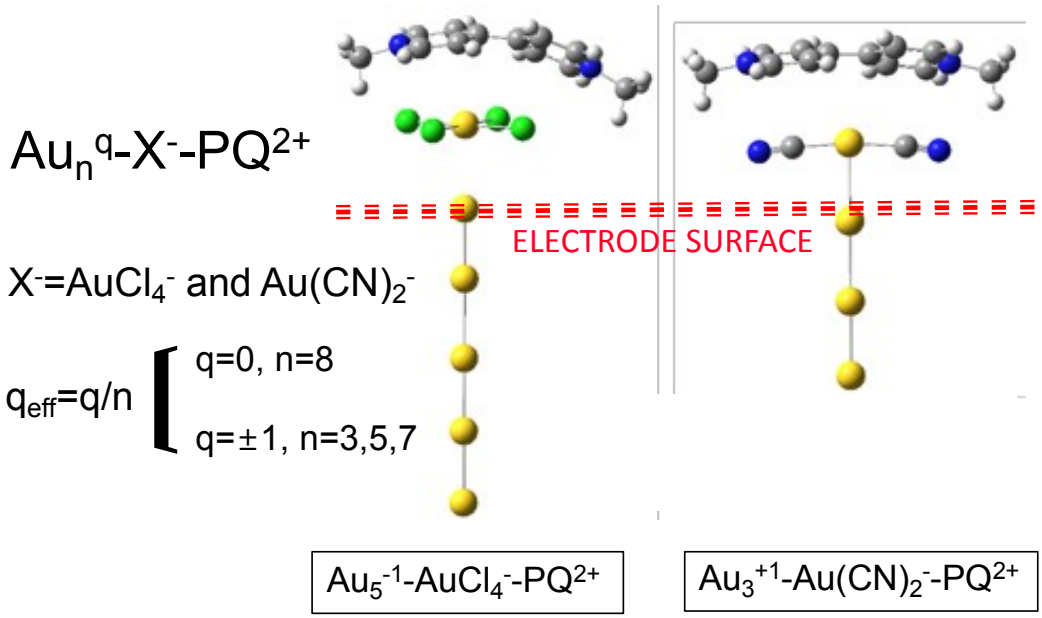

Figure S6. Examples of Au_n^q–X^-–PQ^{2+} molecular models used in the theoretical calculations. Left: Au_5^{-1}–$AuCl_4^-$–PQ^{2+} (q_{eff} = q/n = −0.20 a.u.). Right: Au_3^{+1}–$Au(CN)_2^-$–PQ^{2+} (q_{eff} = +0.33 a.u.).

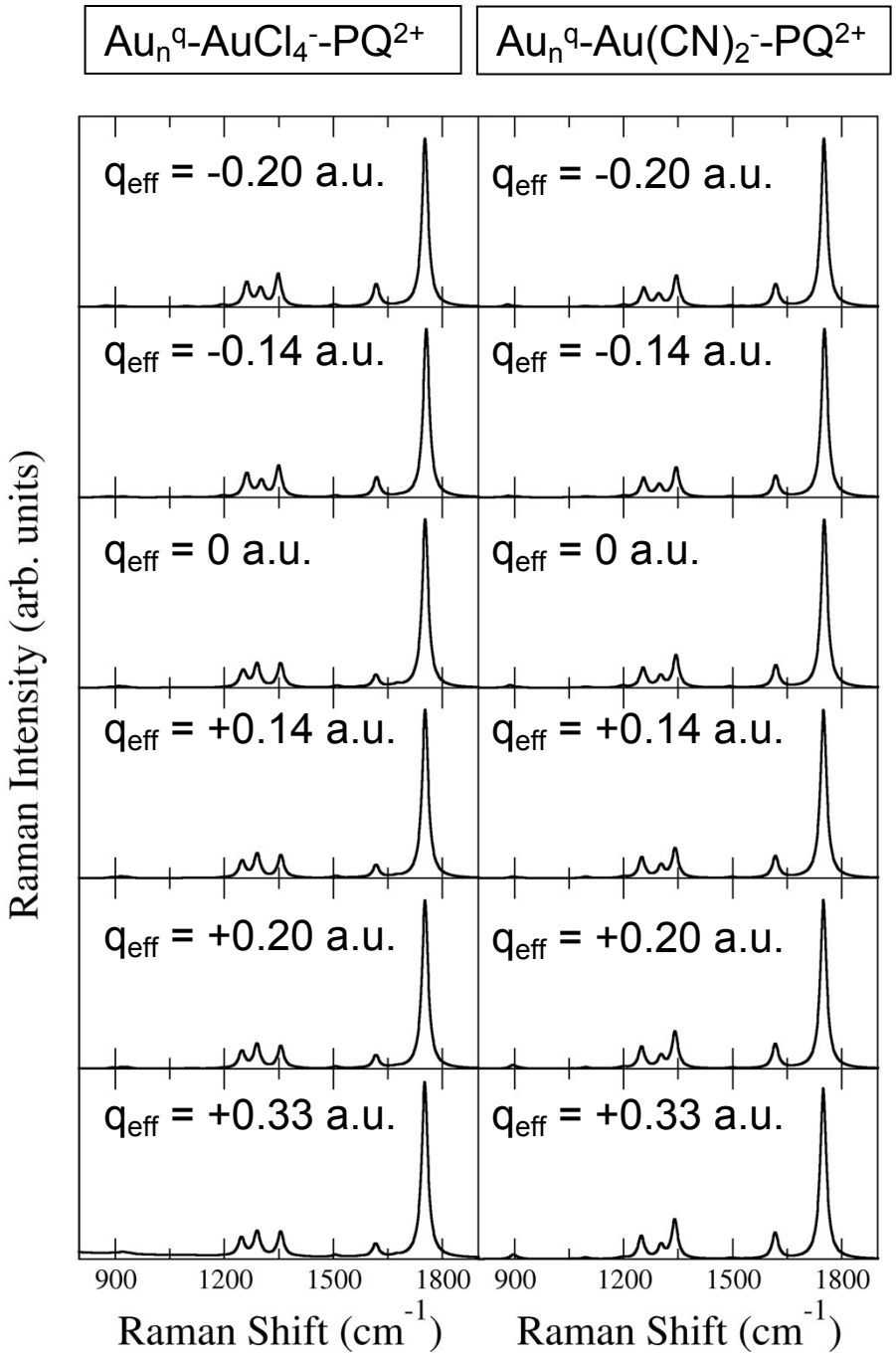

Figure S7. Theoretical SERS-CT spectra in resonance with the metal-to-molecule CT excited states (Figure 4) of Au_n^q–$AuCl_4^-$–PQ^{2+} and Au_n^q–$Au(CN_2)^-$–PQ^{2+} supermolecules calculated from TD-M06-HF/LanL2DZ results at different densities of charge $q_{\text{eff}} = q/n$ (unscaled wavenumbers).

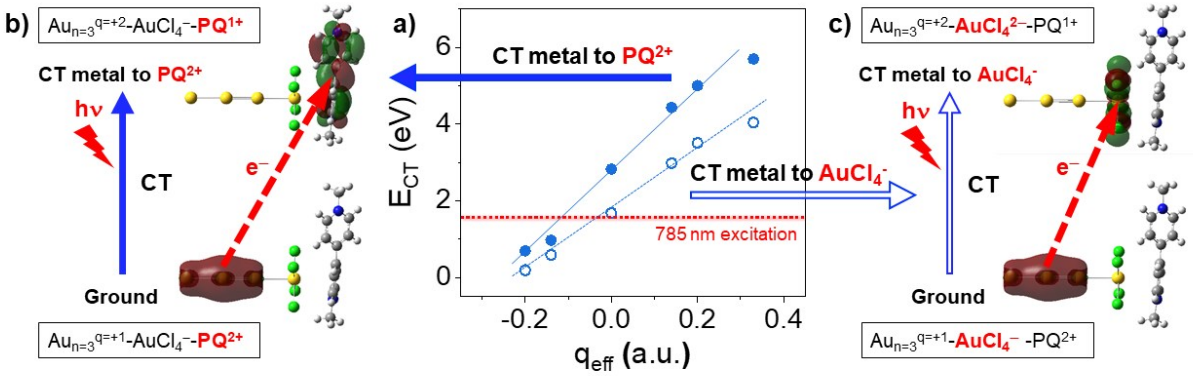

Figure S8. (a) Dependence of the TD-M06-HF/LanL2DZ calculated energies of the metal-to-PQ^{2+} (full) and metal-to-$AuCl_4^-$ (empty) CT excited states on the density of charge ($q_{eff} = q/n$) of the Au_n^q–$AuCl_4^-$–PQ^{2+} supermolecule. Example of the orbitals involved in the photo-induced CT excitation of a single electron from the HOMO of the Au_n^q clusters (b) to the LUMO of paraquat or (c) to the LUMO of $AuCl_4^-$ in the $Au_{n=3}^{q=+1}$–$AuCl_4^-$–PQ^{2+} system.

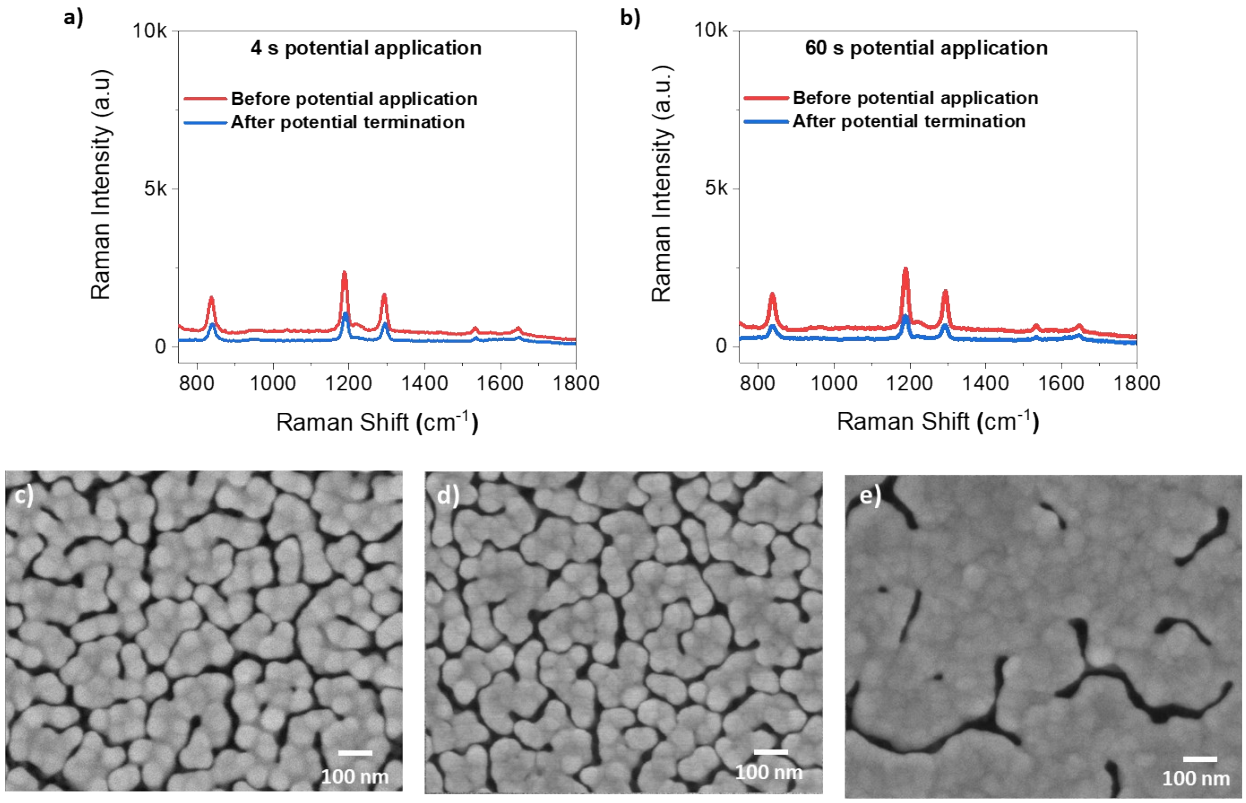

Figure S9. (a,b) EC-SERS spectra of PQ^{2+} (5 μM) recorded at the OCP in the presence of $AuCl_4^-/Cl^-$ (1 mM/0.1 M) before (red) and after (blue) an electrode potential of +0.1 V was applied for (a) 4 s and (b) 60 s. Scanning electron microscopy images of the Au nanopillar substrate: (c) as prepared and after +0.1 V was applied for (d) 4 s and (e) 60 s. The surface morphology after 4 s of applied potential (when maximum enhancement of SERS was achieved) clearly did not differ from the morphology of the original substrate, although the presence of new small nanoparticles cannot be ruled out. The morphology after 60 s showed the formation of a Au film layer on the nanopillar surface due to the reduction of $AuCl_4^-$. If the surface reconstruction and the existence of new generated nanoparticles contribute to enhancing the signals, SERS intensities after the electrode potential treatment should be stronger than those recorded before it was applied. However, SERS spectra recorded after potentials were applied are weaker. This result implies that $AuCl_4^-$ reduction does not substantially contribute to the SERS enhancement.

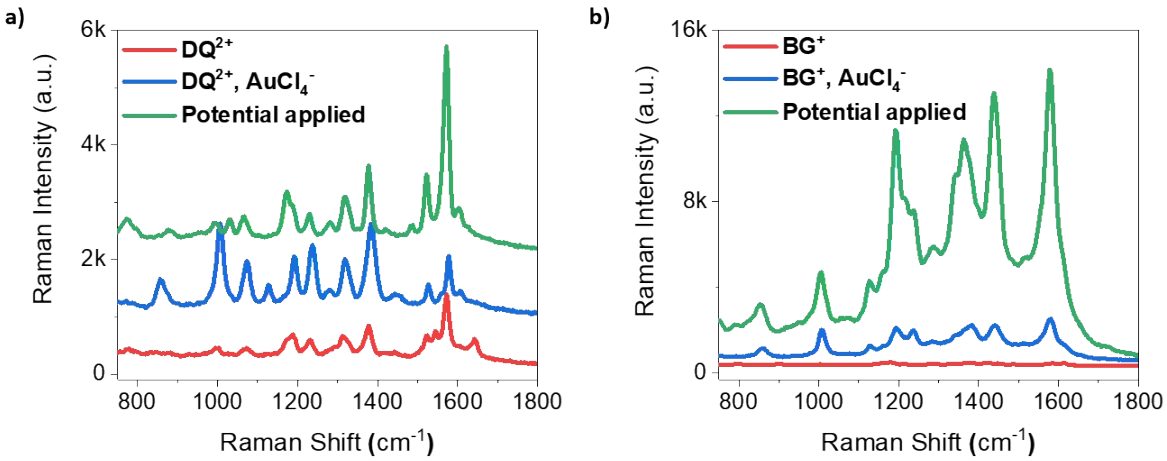

Figure S10. EC-SERS spectra of (a) diquat (DQ^{2+}, 5 μM) and (b) brilliant green (BG^{+}, 5 μM) without (red) and with (blue) the addition of $AuCl_4^-$ (1 mM) before and during (green) the application of electrode potentials of +0.1 and −0.5 V in the cases of DQ^{2+} and BG^{+}, respectively. The presence of $AuCl_4^-$ enhances the SERS spectra (blue) of DQ^{2+} and BG^{+}, which are further amplified 3 and 12 times (green), respectively, under the applied potentials.

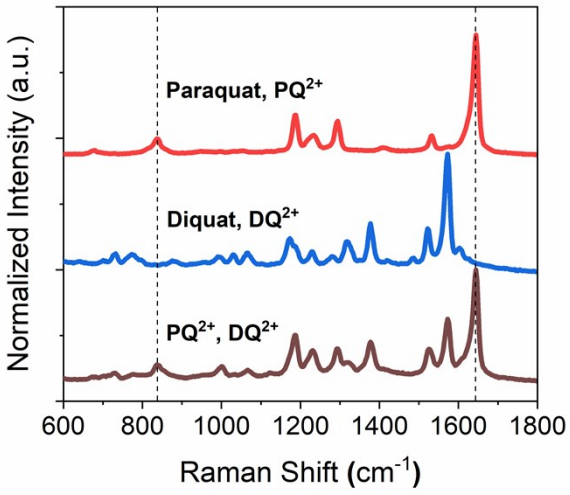

Figure S11. EC-SERS spectra of 5 μM PQ^{2+} (red), 5 μM DQ^{2+} (blue), and their mixture (brown) in the presence of 1 mM $AuCl_4^-$ (in 0.1 M NaCl) at +0.1 V. The vertical dashed lines represent the characteristic paraquat peaks that do not overlap with DQ^{2+} peaks.

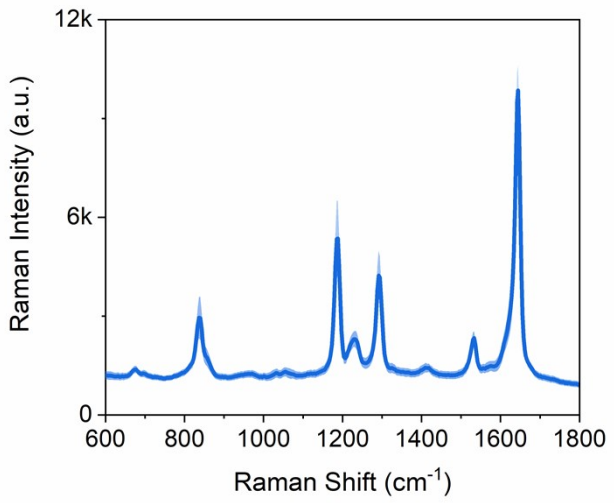

Figure S12. Averaged EC-SERS spectrum of 5 μM PQ^{2+} in the presence of 1 mM $AuCl_4^-$ (in 0.1 M NaCl) at +0.1 V, calculated from 12 spectra measured independently from 12 different Au nanopillar substrates (the shade indicates the standard deviation of Raman intensities). Relative standard deviation with respect to the PQ^{2+} peak at 1639 cm^{-1} is ±7.24%.

References

1) Gaussian 16, Revision A.03, M. J. Frisch, G. W. Trucks, H. B. Schlegel, G. E. Scuseria, M. A. Robb, J. R. Cheeseman, G. Scalmani, V. Barone, G. A. Petersson, H. Nakatsuji, X. Li, M. Caricato, A. V. Marenich, J. Bloino, B. G. Janesko, R. Gomperts, B. Mennucci, H. P. Hratchian, J. V. Ortiz, A. F. Izmaylov, J. L. Sonnenberg, D. Williams-Young, F. Ding, F. Lipparini, F. Egidi, J. Goings, B. Peng, A. Petrone, T. Henderson, D. Ranasinghe, V. G. Zakrzewski, J. Gao, N. Rega, G. Zheng, W. Liang, M. Hada, M. Ehara, K. Toyota, R. Fukuda, J. Hasegawa, M. Ishida, T. Nakajima, Y. Honda, O. Kitao, H. Nakai, T. Vreven, K. Throssell, J. A. Montgomery, Jr., J. E. Peralta, F. Ogliaro, M. J. Bearpark, J. J. Heyd, E. N. Brothers, K. N. Kudin, V. N. Staroverov, T. A. Keith, R. Kobayashi, J. Normand, K. Raghavachari, A. P. Rendell, J. C. Burant, S. S. Iyengar, J. Tomasi, M. Cossi, J. M. Millam, M. Klene, C. Adamo, R. Cammi, J. W. Ochterski, R. L. Martin, K. Morokuma, O. Farkas, J. B. Foresman, and D. J. Fox, Gaussian, Inc., Wallingford CT, 2016.
2) Becke, A. D. Density-functional thermochemistry. III. The role of exact exchange. *J. Chem. Phys*, **1993**, 98, 5648-5652
3) Lee, C.; Yang, W.; Parr, R. G. Development of the Colle-Salvetti correlation-energy formula into a functional of the electron density. *Phys. Rev. B*, **1988**, 37, 785-789.
4) Vosko, S. H.; Wilk, L.; Nusair, M. Accurate spin-dependent electron liquid correlation energies for local spin density calculations: a critical analysis. *Can. J. Phys*., **1980**, 58, 1200-1211.

5) Zhao Y.; D. G. Truhlar, D. G. Comparative DFT study of van der Waals complexes: Rare-gas dimers, alkaline-earth dimers, zinc dimer, and zinc-rare-gas dimers. *J. Phys. Chem*., 2006, 110, 5121-5129.
6) Zhao, Y.; Truhlar, D. G. Density Functional for Spectroscopy: No Long-Range Self-Interaction Error, Good Performance for Rydberg and Charge-Transfer States, and Better Performance on Average than B3LYP for Ground States. *J. Phys. Chem. A*, **2006**, 110, 13126-13130.
7) Dunning Jr., T. H.; Hay, P. J., in *Modern Theoretical Chemistry*, Ed. H. F. Schaefer III, Vol. 3 (Plenum, New York, 1977) 1-28.
8) Hay, P. J.; Wadt, W. R. Ab initio effective core potentials for molecular calculations - potentials for the transition-metal atoms Sc to Hg. *J. Chem. Phys*., **1985**, 82, 270-83.
9) Wadt, W. R.; Hay, P. J. Ab initio effective core potentials for molecular calculations - potentials for main group elements Na to Bi**.** *J. Chem. Phys*.,**1985**, 82, 284-98.
10) Hay, P. J.; Wadt, W. R. Ab initio effective core potentials for molecular calculations - potentials for K to Au including the outermost core orbitals. *J. Chem. Phys*., 1985, 82, 299-310.
11) Long, D.A. The Raman Effect: A Unified Treatment of the Theory of Raman Scattering By Molecules, Wiley, 2002
12) Santoro, F.; Cerezo, J. FCclasses3, a code for vibronic calculations. Available upon request. 2019
13) Avila Ferrer, F. J.; Santoro, F. Comparison of vertical and adiabatic harmonic approaches for the calculation of the vibrational structure of electronic spectra. *Phys. Chem. Chem. Phys*., **2012**,14, 13549–13563
14) Avila Ferrer, F. A.; Fernandez, D. J.; Arenas, J. F.; Otero, J. C.; Soto, J. Modelling the effect of the electrode potential on the metal–adsorbate surface states: relevant states in the charge transfer mechanism of SERS. *Chem. Commun*., **2011**,47, 4210-4212.
15) Avila, F.; Ruano, C.; Lopez-Tocon, I.; Arenas, J. F.; Soto, J.; Otero, J. C. How the electrode potential controls the selection rules of the charge transfer mechanism of SERS. *Chem. Commun*., **2011**,47, 4213-4215.
16) Roman-Perez, J.; López-Tocón, I.; Castro, J. L.; Arenas, J. F.; Soto, J.; Otero, J. C. The electronic structure of metal-molecule hybrids in charged interfaces: surface-enhanced Raman selection rules derived from plasmon-like resonances. *Phys. Chem. Chem. Phys*. **2015**, *17*, 2326-2329.
17) Valdivia, S.; Aranda, D.; Avila Ferrer, F. J.; Soto, J; López-Tocón, I.; Otero, J.C. Proving the Dual Electronic Structure of Charged Metal-Molecule Interfaces: Surface-Enhanced Raman Scattering of Cyanide Adsorbed on a Nanostructured Silver Electrode. *J. Phys. Chem. C* **2020**, 124, 17632–17639.
18) Jacobs, M. B.; Jagodzinsko, P. W.; Jones, T. E.; Eberhart, M. E. A Surfaced-Enhanced Raman Spectroscopy and Density Functional Theory Study of $[Au(CN)2]^-$/$[Au(CN)4]^-$ Adsorbed on Gold Nanoparticles. *J. Phys. Chem. C*, **2011**, 115, 24115–24122.